

Mass Composition Studies of the Highest Energy Cosmic Rays

José Bellido, for the Pierre Auger Collaboration

Department of Physics, The Pennsylvania State University, USA^a

The determination of the mass composition of the highest energy cosmic rays is one of the greatest challenges in cosmic ray experiments. The highest energy cosmic rays are only detected indirectly because of their very low flux. Using the atmosphere as a large target, Air Fluorescence Detectors are capable of tracing the evolution of the size of the Extensive Air Shower through the atmosphere (the shower longitudinal profile). The analysis of the characteristics of the detected longitudinal profiles is currently the most reliable way for extracting some information about the primary cosmic ray mass composition. In this proceeding, I will describe in some detail the Pierre Auger elongation rate studies, and I will show the potential for mass composition studies using the surface and the fluorescence detectors information as part of a single analysis. The interpretation of the current data with regard to mass composition, relies heavily on high energy hadron interaction models. Using standard hadron interaction models, the data suggest that the composition becomes lighter up to about 2×10^{18} eV and above that it becomes heavier again. This apparent change in the mass composition at 2×10^{18} eV seems to be correlated with a spectrum index change in the observed energy spectrum.

1 Introduction

Energetic cosmic rays interacting with the atmosphere initiate a cascade of secondary particles known as an Extensive Air Shower (EAS) that travels near the speed of light. The number of particles existing in the EAS changes as it evolves through the atmosphere. The EAS can be considered to be composed of hadrons, muons and an electromagnetic component. Each of these components evolve differently through the atmosphere.

The number of particles in the EAS (or shower size) as a function of the atmosphere slant depth is called the shower longitudinal profile. Most of the EAS energy is dissipated through the electromagnetic component (where N_e is the number of e^\pm). Therefore, the shower size (N_e) increases until the average energy of the e^\pm in the EAS is about the critical energy ($E_c = 81$ MeV). The critical energy is when the rate of energy loss due to collisions and ionization begins to exceed that due to radiation. This happens when the energy of e^\pm is smaller than the energy lost by ionization (2.2 MeV/g/cm²) after traveling one radiation length (37 g/cm² in air). A radiation length is the grammage path length required so that the energy of e^\pm is attenuated by the factor $1/e$ due to bremsstrahlung radiation. Photons attenuate to $1/e$ due to pair production within a similar grammage path length¹.

The slant depth at which the longitudinal profile reaches its maximum is called X_{max} and this is the main shower parameter used to extract information about the mass composition of the primary cosmic ray.

^aCurrently at: Physics Department, The University of Adelaide, SA-5005, Australia

The EAS initiated by a higher energy cosmic ray has more energy to dissipate, so it takes longer for the particles to reach the critical energy. Therefore, for a given composition, the average X_{max} should increase as a function of the cosmic ray energy. On the other hand, heavier nuclei can be considered as the superposition of many nucleons. For an iron nucleus with energy E , each nucleon would have energy $E/56$, and the superposition of 56 lower energy subshowers will reach X_{max} earlier (higher in the atmosphere). In the superposition model, because each nucleon has a smaller energy, secondary pions reach sooner (than a single nucleon with energy E) to lower energies where they can decay to muons instead of transferring energy to the electromagnetic cascade¹. Then heavier nuclei will produce more muons than lighter nuclei and they will also reach X_{max} higher in the atmosphere (smaller X_{max}). Figure 1 shows the expected shower profiles for proton and iron showers according to MC simulations.

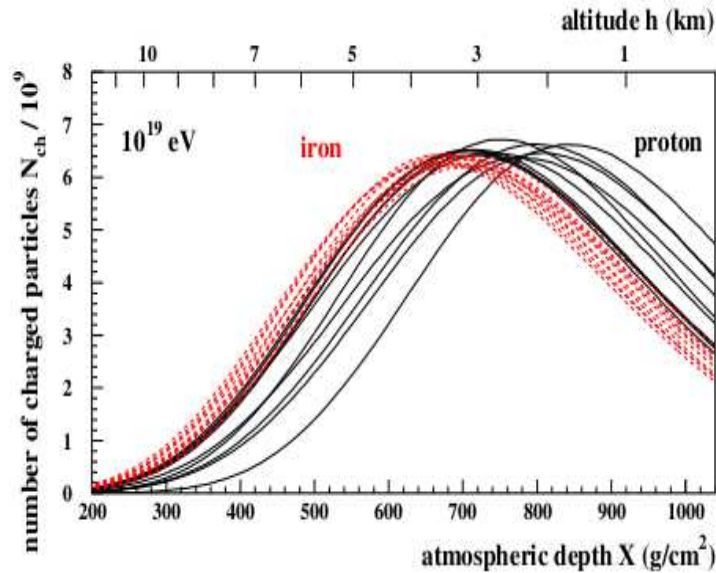


Figure 1: Individual longitudinal shower profiles for 10^{19} eV proton (solid black lines) and iron (dashed red lines) vertical showers according to MC simulations².

Proton and iron showers not only have their average X_{max} values at somewhat different slant depths, but also their X_{max} fluctuations are different. Figure 2 shows the distribution of X_{max} for fixed-energy proton and iron showers according to MC simulations. Iron showers have a narrower distribution.

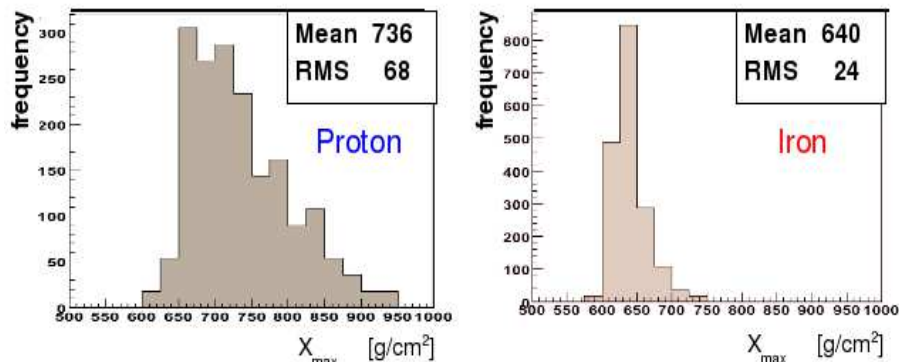


Figure 2: Expected distributions for X_{max} for 10^{18} eV proton and iron showers according to MC simulations using the QGSJET model for high energy hadron interactions.

Experimentally, there are some issues when measuring the muon abundance. The muon abundance is only measured at ground level (where the ground particle detectors are deployed). The relative abundance of muons at the ground is therefore also dependent on the particular zenith angle of the shower. Another issue is that, depending on the relative location of each ground particle detector, they will sample the muon content at different ages of the shower development (except for vertical showers). Furthermore, efficiently separating the muon content from the electromagnetic signal requires more complex detector systems (i.e. detectors buried underground). However, fluorescence detectors have the capability to track the shower development through the atmosphere and X_{max} is measured with good accuracy. In this proceeding I will focus on mass composition studies based on X_{max} observations with the fluorescence detector (FD) of the Pierre Auger Observatory.

2 Shower Reconstruction and Resolution on X_{max}

The Pierre Auger Observatory is a hybrid cosmic ray detector³. It uses ground particle detectors to sample the shower cascade particles at the ground and also fluorescence detectors to track the shower development through the atmosphere. Figure 3 shows the layout of the the ground detectors (or stations) and the layout of the fluorescence detectors . There are 1600 stations spaced by 1.5 km and covering a total area of about 3000 km². There are also four fluorescence detectors (Los Leones, Los Morados, Loma Amarilla and Coihueco) located at the edges of the array and overlooking the array as indicated in figure 3.

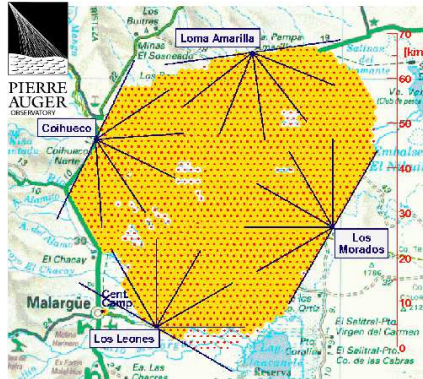


Figure 3: Layout of the Pierre Auger Observatory.

Each fluorescence detector is a building that contains six telescopes. Each telescope uses a spherical mirror to focus the light onto a camera. The camera is formed by 440 hexagonal PMTs (or pixels) and the angular size of each pixel is 1.5° . The total field of view of the camera is approximately 28° elevation by 30° azimuth³.

Figure 4 shows an example of a EAS seen by the fluorescence detector and also detected by the ground array (hybrid event). The figure on the left (fig. 4) shows the shower track crossing through the camera field of view. The figure on the right shows the shower axis landing on the surface array, the larger circles show the stations triggered by the shower.

The uncertainty in the reconstructed shower geometry is much smaller for hybrid events. The time and location information from the station closest to the shower core is a powerful constraint on the reconstructed shower geometry. On average, the uncertainty in the hybrid reconstructed arrived direction is about 0.6° ⁴. For mass composition studies we use only hybrid events (events that triggered only the FD have a poorer geometry resolution, and therefore, poorer X_{max} resolution).

Once the shower geometry is determined, the shower longitudinal profile is estimated. The

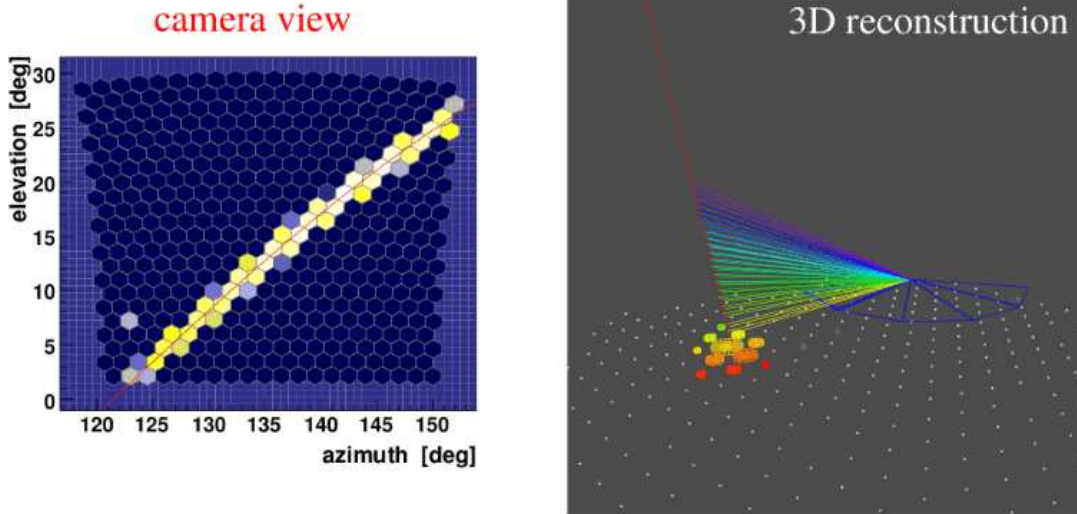


Figure 4: On the left: Example of a Cosmic Ray seen by the Fluorescence Detector. On the right: The same event seen in 3D. The dots denote the location of the surface detectors and the larger circles are for the stations that were triggered by this event.

longitudinal profile can be estimated as N_e (shower size) or as dE/dX (deposited energy) as a function of slant depth. In the Pierre Auger Observatory we estimate dE/dX as a function of slant depth⁵. Figure 5 shows the reconstructed longitudinal profile for the same event shown in figure 4. The integral of dE/dX provides the total energy that is deposited in the atmosphere (E_{tot}), and the total energy contained by the primary cosmic ray is obtained after a correction to account for the missing energy (energy that is not dissipated in the atmosphere). The missing energy correction is both model dependant and primary mass composition dependant. The range of this correction is about 10%^{6,7}.

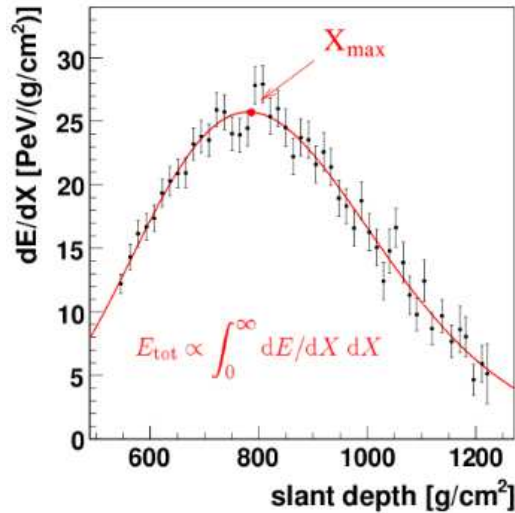


Figure 5: Reconstruction of the shower profile from the event seen in figure 4.

The function used to fit the observed longitudinal profile (red line in figure 5) is the Gaisser-Hillas function⁸, shown in equation 1. It has four free parameters: X_{max} , $(dE/dX)_{max}$ (or N_{max} when the longitudinal profile is in terms of N_e), λ and X_0 . X_{max} is the slant depth where the shower reached its maximum size, and $(dE/dX)_{max}$ is the energy deposited at X_{max} . The

other two parameters λ and X_0 , are shape parameters. λ relates to the width of the profile and X_0 to the start of the profile. Even though X_0 relates to the start of the profile, it is not to be interpreted as the depth of the first interaction, since it often takes negative values when fitting simulated showers and also real showers.

$$dE/dX = (dE/dX)_{max} \left(\frac{X - X_0}{X_{max} - X_0} \right)^{\frac{X_{max} - X_0}{\lambda}} e^{-\frac{X_{max} - X_0}{\lambda}} \quad (1)$$

The uncertainty in the reconstructed X_{max} in a given event depends on how large a fraction of the profile is seen by the FD, and whether X_{max} is inside this fraction of the profile. We use MC events to estimate the uncertainty in the reconstructed X_{max} as a function of the observed grammage length. Figure 6 (plot on the right) shows the uncertainties for showers with X_{max} bracketed^b (solid circles), and for not bracketed showers (solid triangles). For a cross check of the X_{max} uncertainty estimates we selected real showers where the entire profile is seen by the FD (like the one shown in figure 5). The uncertainty in the reconstructed X_{max} is small ($< 20 \text{ g/cm}^2$) for such showers. This reconstructed X_{max} is considered as the true value, a new X_{max} reconstruction is performed (basically a new fit to the Gaisser-Hillas function) but this time using only a smaller fraction of the observed profile, but still with X_{max} within this fraction (left plot in figure 6). The uncertainty of the reconstructed X_{max} estimated using real showers is shown with open circles in figure 6. It is consistent with the X_{max} uncertainty estimated using MC events.

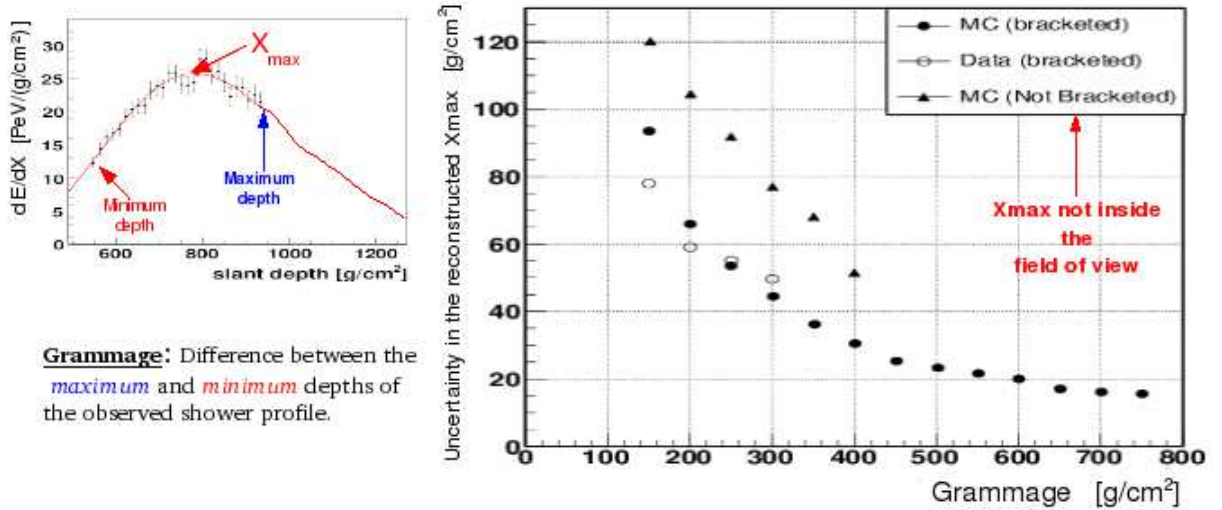


Figure 6: Estimated resolution on the reconstructed X_{max} as a function of the observed grammage length (plot on the right). The plot on the left shows the start (minimum depth) and the end (maximum depth) of the fraction of the shower profile seen by the FD (region with data points).

For mass composition analysis we want to use only showers where X_{max} is reconstructed with an uncertainty smaller than 40 g/cm^2 . This small uncertainty is achieved by rejecting showers with grammage length smaller than 320 g/cm^2 and showers with X_{max} not being bracketed. The average uncertainty in the reconstructed X_{max} is about 20 g/cm^2 when applying these cuts. High energy showers more often land further away from the FD (compared with low energy showers) and because of the FD limited field of view (see fig. 7) they have larger observed grammage lengths on average. Therefore, the average uncertainty in their reconstructed X_{max} is slightly smaller (than those for lower energy showers).

^b X_{max} bracketed means that the reconstructed X_{max} is within the fraction of the profile seen by the FD

3 The Mean X_{max} and the FD limited Field of View

The FD has a limited field of view in elevation ranging from about 2° to 30° , introducing a bias in the distribution of X_{max} from the observed showers. This bias is amplified by demanding that X_{max} be within the observed profile (X_{max} bracketed). The reason for this bias in the X_{max} distribution is because many showers landing close to the FD will have their X_{max} outside (above) the field of view (see fig 7) and the observed profile will not have a bracketed X_{max} or the shower will simply not be detected. As a result the mean X_{max} will appear to be larger (deeper). A similar bias happen for high energy showers. High energy showers develop their X_{max} deeper in the atmosphere, then for some vertical (or near vertical) showers X_{max} will be below the ground (see fig 7), therefore rejected from the analysis. In this case the mean X_{max} appears to be smaller (shallow).

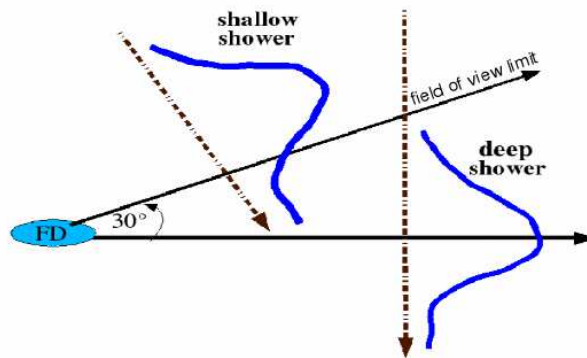


Figure 7: Diagram showing the possible bias in the estimated $\langle X_{max} \rangle$ due to the limited field of view of the Auger fluorescence detector.

In order to avoid the bias in the estimated mean X_{max} , showers with specific geometries relative to the FD are rejected. To identify the optimum shower geometries to be used for determining the mean X_{max} ($\langle X_{max} \rangle$) values, we introduced the parameters X_{up} and X_{low} . These parameters are the lower and upper limits of the slant depth along the shower axis that is inside the FD field of view. These limits may be defined at where the shower axis intercepts the FD field of view limit or where the shower axis intercepts the maximum distance that a shower with energy E is still detectable (as shown in figure 8).

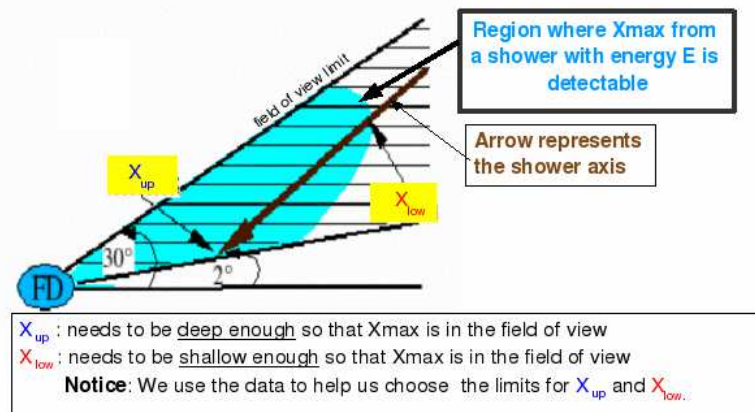


Figure 8: Diagram showing the definition of X_{low} and X_{up} . X_{low} and X_{up} are the lower and upper limits of the slant depth along the shower axis that is inside the FD field of view.

The basic idea is that X_{low} has to be shallow (small) enough, and X_{up} has to be deep (large) enough to guarantee that X_{max} will be within the field of view. Notice that the values for X_{low} and X_{up} depend only on the geometry of the shower and not on the particular depth of the shower profile (but it does also depend in the overall distribution of shower profile depths). In order to determine the optimum ranges for X_{low} and X_{up} as a function of energy we use real data. Figure 9 shows the mean X_{max} as a function of X_{low} (plot on the left) and X_{up} (plot on the right) for different energies. The arrows in figure 9 indicates where the fitted functions start to deviate from being flat and this defines the limit values for X_{low} and X_{up} . The flat region is the unbiased one.

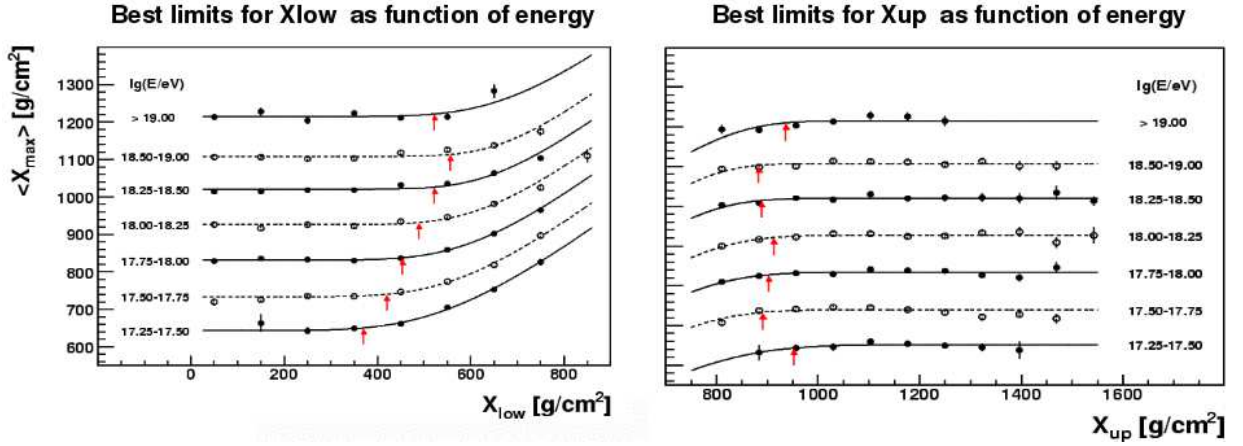


Figure 9: The mean X_{max} values are plotted as a function of X_{low} and X_{up} for each energy range. The limits for the accepted X_{low} and X_{up} values (at each energy range) correspond to the values where the fitted functions start to deviate from being flat. For didactic purposes, the mean X_{max} values are offset by 75 g/cm^2 consecutively.

4 Checking the Anti-Bias Cuts with MC Data

It is possible to check the performance of the cuts applied to X_{low} and X_{up} using MC data. We have simulated MC showers and pass these showers through the detector simulation, where the FD and the SD components are simulated in detail^{9,10}. We then reconstruct all triggered MC showers in the same way as real showers. The input compositions for the MC simulation are pure iron, pure proton, and a mixed composition of 50% iron and 50% proton.

Figure 10 shows that the reconstructed mean X_{max} are consistent with the mean X_{max} from MC inputs. This indicates that the cuts applied on X_{low} and X_{up} efficiently removed the bias in X_{max} . The minimum energy where the mean X_{max} can still be measured (without being biased) is just above $10^{17.5}$ eV. The limits for X_{low} and X_{up} are not the same for all compositions. For each composition we need to follow the procedure described in the previous section. This is because the limits for X_{low} and X_{up} depend on the particular range of the observed (or simulated) X_{max} values.

We also confirm the stability of the X_{max} distributions with respect the quality cuts and the cuts on X_{low} and X_{up} . This is of particular interest since the fluctuations in X_{max} are sensitive to primary mass composition. Figures 11 and 12 show the distributions for X_{max} for proton and iron primaries respectively. The solid lines indicate the reconstructed distributions and the dotted lines indicate the MC input distributions, both distributions are consistent, so the quality cuts and the cuts on X_{low} and X_{up} are not biasing the X_{max} distributions.

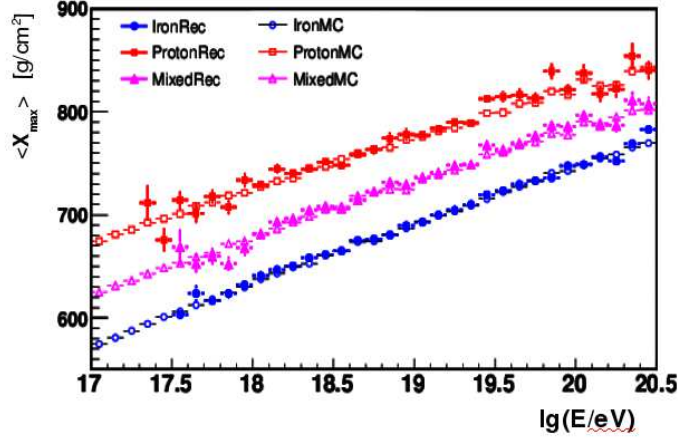


Figure 10: Reconstructed mean X_{max} as a function of energy for MC generated data (solid symbols). The open symbols indicate the true mean X_{max} from the MC input. The simulated primary compositions are proton (squares), iron (circles) and a proton/iron mixed composition (triangles).

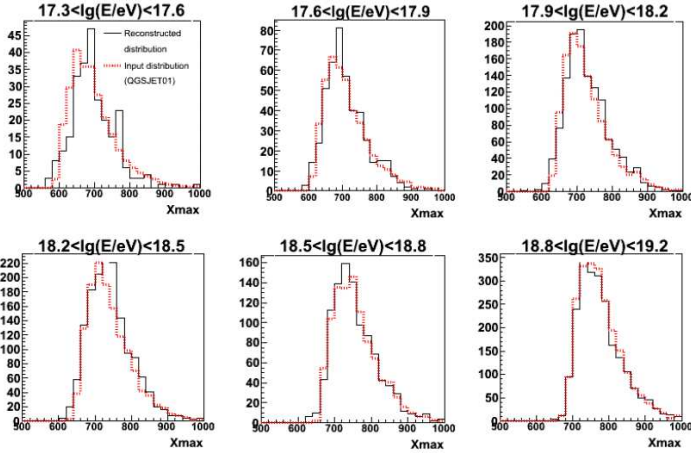


Figure 11: Distributions for **proton** showers at different energy ranges (see caption in figure 12).

5 Results and Discussion

Figure 13 shows the reconstructed mean X_{max} as a function of energy as measured with the Auger data¹¹. The blue and red lines are the expected mean X_{max} values for iron and proton showers respectively for different hadronic interaction models.

The rate that the mean X_{max} increases per decade in energy is known as the *elongation rate*. For a pure composition the expected elongation rate is model dependent and it is about $50 \text{ g/cm}^2/\text{decade}$ (as shown with blue and red lines in figure 13). The plot on the left in figure 14 shows a linear fit to the data ($\langle X_{max} \rangle = A + D_{10} \times \lg E$). The slope of this fit (D_{10}) corresponds to the measurement of the elongation rate ($D_{10} = 54 \pm 2 \text{ g/cm}^2/\text{decade}$). However, the χ^2/Ndf of the fit (24/13) suggest that a straight line may not be the best fit for the entire energy range. The probability that the data will follow a single line is smaller than 3%. The plot on the right in figure 14 shows that a broken line fits better the data. The probability that the data follows a broken line is 63%. The break point according to the fit is at about 2 EeV . The elongation rate below and above 2 EeV is $71 \pm 5 \text{ g/cm}^2/\text{decade}$ and $40 \pm 4 \text{ g/cm}^2/\text{decade}$ respectively¹¹. The uncertainties in the elongation rate measurements come from the fit and do not take into account the systematic uncertainties on the measured mean X_{max} values. The

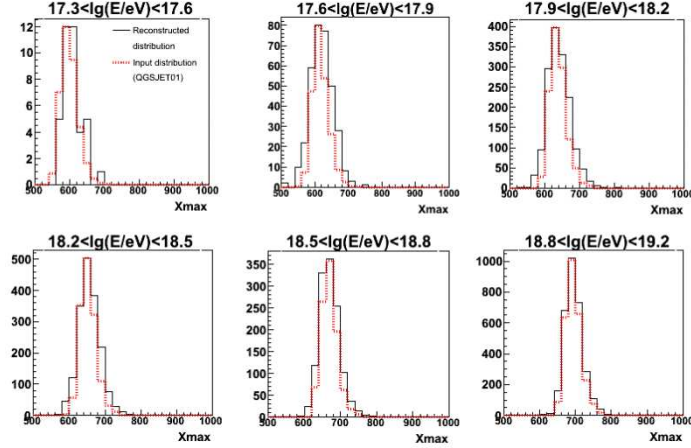


Figure 12: Distribution for **iron** showers at different energy ranges according to MC simulations. The solid (black) lines show the reconstructed X_{max} distributions, and the dotted (red) lines show the MC input X_{max} distributions (using the QGSJET01 model).

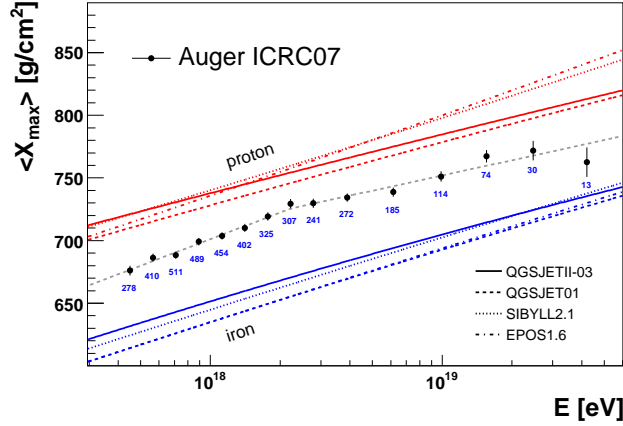


Figure 13: Auger results for the Mean X_{max} measurements as a function of energy¹¹.

systematic uncertainties in the estimated mean X_{max} are larger at lower energies. Below $1 EeV$ the systematic uncertainties are smaller than $15 g/cm^2$ and above $1 EeV$ they are smaller than $12 g/cm^2$.

If the hadron interaction models were entirely correct, we would interpret the large elongation rate result for the energy region below $2 EeV$ ($71 \pm 5 g/cm^2/decade$) as a mixed composition that is becoming lighter with energy, and the small elongation rate result for the energy region above $2 EeV$ ($40 \pm 4 g/cm^2/decade$) as a mixed composition that is becoming heavier with energy. However, this sudden change in the elongation rate at $2 EeV$ may be the result of a high energy hadronic interaction property (instead of a composition change).

Interestingly the energy spectrum presents a change of spectral index at about $2 EeV$. This feature in the energy spectrum is known as the ankle. Figure 15 shows the residuals of the measured cosmic ray flux with respect to a cosmic ray flux with a spectrum of the form $\propto E^{-2.6}$ (black symbols). A spectral index of 2.6 corresponds to the one measured between $2 \times 10^{18} eV$ and $3 \times 10^{19} eV$ ¹², that is why the residuals curve is flat within this region. Outside these energy ranges the measured cosmic ray energy spectrum has a larger spectral index. In the same plot (fig. 15) we show (with red symbols) the residuals of the mean X_{max} with respect to a linear function (in $\lg E$ space) that corresponds to the best fit to the elongation rate data below $2 EeV$

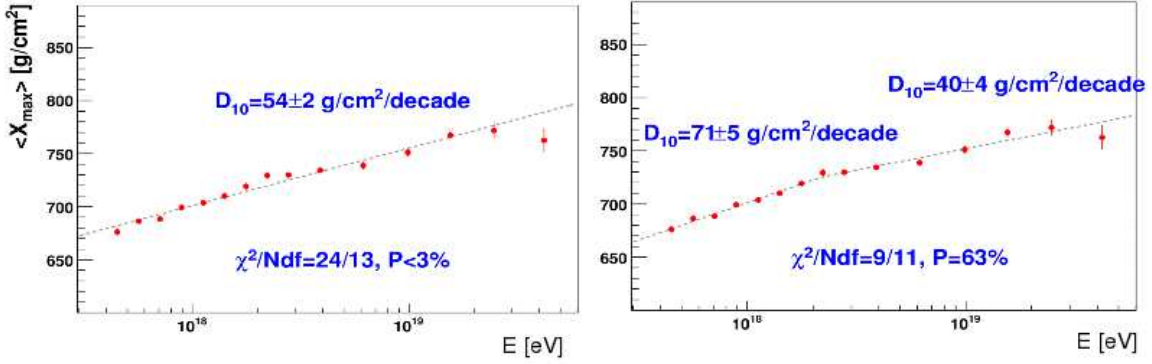


Figure 14: The plot on the left shows a fit to a single line. The plot on the right shows a fit to a broken line¹¹.

(see figure 14, plot on the right). Notice that both residual plots are consistent with a feature at $2 EeV$. Unfortunately there is not yet enough hybrid data to see whether the elongation rate plot has another feature at 3×10^{19} as the energy spectrum does.

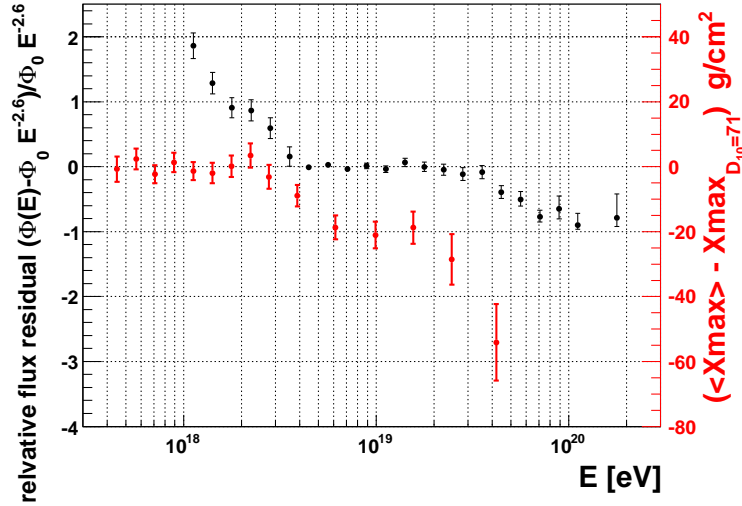


Figure 15: Comparing the features observed in the energy spectrum¹² against the features observed in the elongation rate measurements¹¹.

The consistency between the features observed in the energy spectrum and in the elongation rate at $2 EeV$ suggests that both features have the same origin. Unfortunately, this evidence is not enough to distinguish between a mass composition change or a hadron interaction physics change. However, the consistent features in the energy spectrum and in the elongation rate give us some confidence that the feature observed in the elongation rate is a real effect and not an artifact due to any detection or reconstruction bias.

So far the Pierre Auger collaboration has only presented mass composition studies using the mean X_{max} information. New studies of the elongation rate and also studies of the X_{max} fluctuations should be released soon. As already mentioned earlier in this proceeding, the fluctuations on X_{max} are also sensitive to mass composition. In this new study, the systematic uncertainties on the measured mean X_{max} values may be slightly reduced and the statistics will be larger, allowing us to go up in energy to about 5×10^{19} eV with small statistical uncertainties.

In addition to the X_{max} measurements obtained from the FD, there are other parameters obtained with the SD that are currently being studied. The shape of the traces observed in the PMT located in the tanks (figure 16) and how they change as a function of the azimuth around

the shower axis is correlated with the muon abundance, and therefore with the primary mass composition (as discussed in section 1). A commonly used parameter to characterize the shape of the PMT traces is the rise time^{13,14,15}. The rise time is the time that the traces take to collect 10% to 50% of the total signal (see figure 16). Muons usually travel with the leading edge of the shower front, while the electromagnetic component can have some delay depending on how far from the shower axis is the sampled station. So, a smaller rise time means a larger muon abundance. It was also found that, except for vertical showers, the variation of the rise time around the shower axis is also sensitive to the mass composition (asymmetry studies). The ratio between the signal arriving earlier (within the first 600 ns) over the signal arriving later (signal arriving after 600 ns) is another measurement of the muon/electromagnetic ratio (we called this ratio the *shape parameter*). For stations that are not so close to the shower axis, when a muon is detected, it generates a quite distinguishable peak. Another technique studies the peaks (or bumpiness) on the traces to estimate the muon contribution to the total signal.

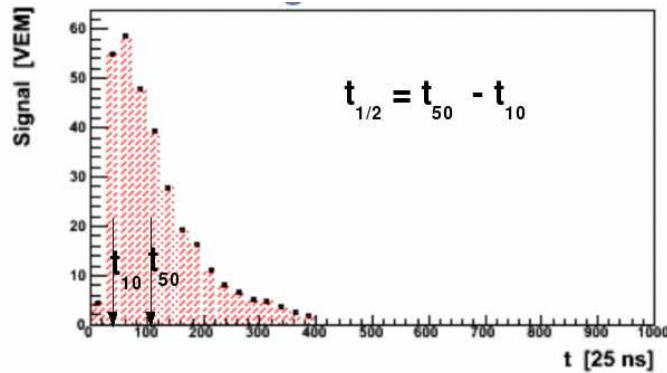


Figure 16: Example of a trace recorded by one PMT located in a surface detector. The arrows indicate the time interval between the arrival of 10% and 50% of the integrated total signal.

The hybrid detection provides an enormous potential for mass composition studies that has not yet been fully exploited. Each of these parameters (rise time, asymmetry studies, shape parameter and muon abundance) may provide an independent measurement of the mass composition with independent sources of systematics, and since all these parameters were extracted from a common event, a multiparameter analysis of the mass composition may also be possible.

6 Conclusions

We have presented the latest Auger results regarding the mass composition studies¹¹. According to standard hadronic interaction models and the current elongation rate results, the cosmic ray composition is a mixed composition that is becoming lighter with energy up to 2 EeV . Above 2 EeV the cosmic ray composition changes its trend and starts to become heavier with energy (see figure 14 plot on the right). The mass composition breaking point at 2 EeV correlates with a change in the spectral index of the cosmic ray energy spectrum (figure 15).

There is not a unique interpretation for the breaking point in the elongation rate data. It may be that the breaking point is not related with a mass composition change, but with a change in hadronic interaction physics. A sudden change in the hadronic interaction physics would have an effect on the expected signal at the ground for a given shower energy. This would cause a systematic error in the reconstructed shower energy. Therefore, an artificial break in the energy spectrum could arise due to a sudden change in the hadronic interaction physics.

There have been previous studies of the elongation rate by other fluorescence detectors^{16,17,18}. Figure 17 shows that there are some systematic differences at lower energies (below 2 EeV)

among different experiments, but for higher energies all the experiments are consistent within their uncertainties. Above 2×10^{19} eV the other experiments run out of statistics, and Auger has still some more measurements. The last two energy bins (in the Auger data) suggest a trend towards heavier composition (according to standard hadronic interaction models).

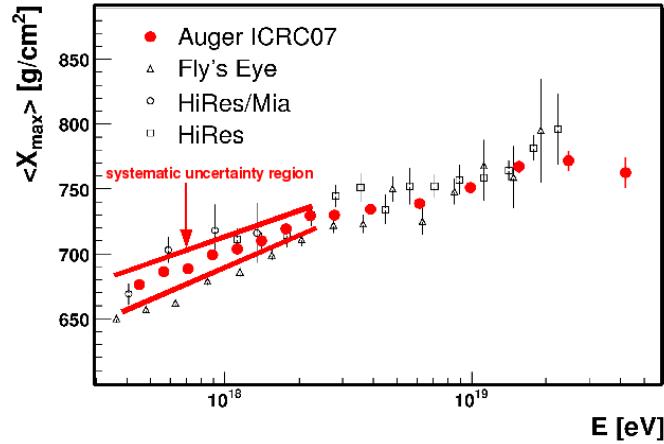


Figure 17: Comparing the mean X_{max} measurements from the Pierre Auger Observatory with previous measurements^{16,17,18}.

Acknowledgments

The author wish to thanks to the organizers of the XXth Rencontres de Blois 2008 “Challenges in Particle Astrophysics” for their invitation to present this work.

References

1. P. Sommers, C. R. Physique 5, 463 (2004).
2. M. Risse, Acta Phys.Polon. **B35** ,1787, (2004), arXiv:astro-ph/0402300v1.
3. J. Abraham *et al* [Pierre Auger Collaboration], *Nucl. Instrum. Methods* **A523**, 50 (2004).
4. C. Bonifazi *et al* [Pierre Auger Collaboration], Proc. 29th ICRC, , Pune, **7**, 17, (2005).
5. M. Unger *et al*, *Nucl. Instrum. Methods* **A588**, 433 (2008).
6. H.M.J. Barbosa *et al*, *Astropart. Phys.* **22**, 159 (2004).
7. T. Pierog *et al* , Proc. 29th ICRC, , Pune, **7**, 103, (2005). Proc. 30th ICRC, , Merida, (2007), arXiv:0802.1262 [astro-ph].
8. T. Gaisser, M. Hillas, Proc. 15th ICRC, , Plodiv, **8**, 353, (1977).
9. S. Argiro *et al*, *Nucl. Instrum. Methods* **A580**, 1485 (2007).
10. L. Prado *et al*, *Nucl. Instrum. Methods* **A545**, 632 (2005).
11. M. Unger, *et al* [Pierre Auger Collaboration], Proc. 30th ICRC, , Merida, (2007), arXiv:0706.1495v1 [astro-ph].
12. M. Roth, *et al* [Pierre Auger Collaboration], Proc. 30th ICRC, , Merida, (2007), arXiv:0706.2096v1 [astro-ph].
13. Watson, A. A., and J. G. Wilson, *J. Phys. G* **7**, 1199 (1974).
14. Walker, R., and A. A. Watson, *J. Phys. G* **7**, 1297 (1981).
15. Walker, R., and A. A. Watson, *J. Phys. G* **8**, 1131 (1982).
16. D.J. Bird *et al* [Fly’s Eye Collaboration], *Phys. Rev. Lett.* **71**, 3401 (1993).
17. T. Abu-Zayyad. *et al* [HiRes-MIA Collaboration], *Astrophys. J.* **557**, 686 (2001).
18. R.U Abbasi *et al* [HiRes Collaboration], *Astrophys. J.* **622**, 910 (2005).